

# MAPS OF EVOLVING CLOUD STRUCTURES IN LUHMAN 16AB FROM HST TIME-RESOLVED SPECTROSCOPY.

THEODORA KARALIDI

Steward Observatory, Department of Astronomy, University of Arizona, 933 N. Cherry Ave, Tucson, AZ 85721, USA,  
 tkaralidi@email.arizona.edu

DÁNIEL APAI

Steward Observatory, Department of Astronomy, The University of Arizona, 933 N. Cherry Ave, Tucson, AZ 85721, USA  
 Lunar and Planetary Laboratory, University of Arizona, 1629 E University Blvd, AZ 85721, USA  
 Earths in Other Solar Systems Team

MARK S. MARLEY

NASA Ames Research Center, MS-245-3, Moffett Field, CA 94035, USA

ESTHER BUENZLI

Institute for Astronomy, ETH Zürich, Wolfgang-Pauli-Str. 27, 8093 Zürich, Switzerland  
 Draft version August 29, 2018

## ABSTRACT

WISE J104915.57-531906.1 is the nearest brown dwarf binary to our Solar system, consisting of two brown dwarfs in the L/T transition: Luhman 16A & B. In this paper we present the first map of Luhman 16A, and maps of Luhman 16B for two epochs. Our maps were created by applying *Aeolus*, a Markov–Chain Monte Carlo code that maps the top-of-the-atmosphere (TOA) structure of brown dwarf and other ultracool atmospheres, to light curves of Luhman 16A & B using the Hubble Space Telescope’s G141 and G102 grisms. *Aeolus* retrieved three or four spots in the top-of-the-atmosphere of Luhman 16A & B, with a surface coverage of 19%–32% (depending on an assumed rotational period of 5 hr or 8 hr) or 21%–38.5% (depending on the observational epoch) respectively. The brightness temperature of the spots of the best-fit models was  $\sim 200$  K hotter than the background TOA. We compared our Luhman 16B map with the only previously published map. Interestingly, our map contained a large, cooler ( $\Delta T \sim 51$  K) than the background TOA spot that lay at low latitudes, in agreement with the previous Luhman 16B map. Finally, we report the detection of a feature reappearing in Luhman 16B light curves that are separated by tens of hundreds of rotations from each other. We speculate this feature is related to TOA structures of Luhman 16B.

*Subject headings:* methods: statistical - techniques: photometric - stars: WISE J104915.57-531906.1

## 1. INTRODUCTION

WISE J104915.57-531906.1, also known as Luhman 16AB (Luhman 2013), is the nearest brown dwarf binary to our Solar system, at a distance of  $1.9980 \pm 0.0004$  pc (Sahlmann & Lazorenko 2015). Luhman 16AB is composed of two brown dwarfs in the L/T transition: Luhman 16A, an  $L8 \pm 1$  [L7.5] dwarf and Luhman 16B a  $T1.5 \pm 2$  [T0.5] dwarf (Knizhev et al. (2013) [Burgasser et al. (2013)]). Luhman 16B has a rotational period of  $4.87 \pm 0.01$  hr (Gillon et al. 2013), or  $5.05 \pm 0.10$  hr (Burgasser et al. 2014), and an inclination  $i < 30^\circ$  (Crossfield et al. 2014). Buenzli et al. (2015b) using HST observations, reported a rotational period between 4.5 and 5.5 hr for Luhman 16A, while ground-based, spatially resolved observations by Mancini et al. (2015) suggested a longer,  $\sim 8$  hr rotational period. The latter, is longer than the maximum rotational period suggested by  $v \sin i$  observations by Crossfield et al. (2014), assuming a  $\sim 1R_{Jup}$  radius (see, Buenzli et al. 2015b). Luhman 16A has a yet undefined inclination. Faherty et al. (2014) using bolometric luminosities found that the two components have a similar  $T_{eff}$  (Luhman 16A:  $1310 \pm 30$  K and Luhman

16B:  $1280 \pm 75$  K), consistent with previous observations by Knizhev et al. (2013).

Gillon et al. (2013) performed partially resolved observations of Luhman 16AB over multiple rotations and reported strong night-to-night variations of the observed light curves and a large peak-to-peak amplitude ( $\sim 10\%$ ). Resolved observations showed that Luhman 16B is responsible for the observed variability (Biller et al. 2013; Burgasser et al. 2014; Buenzli et al. 2015a), while Luhman 16A did not appear variable above  $\sim 0.4\%$  (see, e.g., Buenzli et al. 2015a). Resolved observations by Burgasser et al. (2013) showed that both components are red and underluminous in the J-band, supporting the idea that clouds are responsible for the observed light curve variability. Later observations by Buenzli et al. (2015b) using the Hubble Space Telescope (HST)/WFC3 G102 grism reported a significant variability for both Luhman 16A (peak-to-peak amplitude of  $\sim 4.5\%$ ) and 16B (peak-to-peak amplitude of  $\sim 9.3\%$ ), cautioning about the implications this has to the unambiguous characterization of the two components in unresolved observations.

Radigan et al. (2014) and Radigan (2014) found that  $39^{+16}_{-14}\%$  of brown dwarfs in the L/T transition are variable, and showed that high-amplitude variability ( $\gtrsim 2\%$ ) is uncommon in the L/T transition ( $24^{+11}_{-9}\%$ ). Metchev et al. (2015) reached a similar conclusion showing that few L/T dwarfs have amplitudes larger than 1%–2%. The fact that both Luhman 16A and B present high-amplitude variability makes this brown dwarf binary a unique object. Buenzli et al. (2015b) performed a statistical analysis and found that the combined probability for Luhman 16A and B to be both variable is  $\lesssim 10\%$ . The reason why both components present a large amplitude variability is yet unclear.

Crossfield et al. (2014) used Doppler imaging to produce the first global map of Luhman 16B. This first map indicated a complex cloud structure, with darker and brighter areas across the globe, which Crossfield et al. (2014) interpreted as observations of thinner and thicker clouds that allowed the observations to penetrate deeper or shallower in the atmosphere. This is in agreement with the general picture suggested by e.g., Apai et al. (2013) for other early T-dwarfs.

In Karalidi et al. (2015) we presented *Aeolus*, a Markov Chain Monte Carlo (MCMC) code that can map the top-of-the-atmosphere (hereafter, TOA) structure of an ultracool atmosphere, per observational wavelength, using observed rotational light curves. In Section 3 we present a brief description of *Aeolus*. For a detailed description of *Aeolus*, and its validation, we refer the reader to Karalidi et al. (2015).

In this paper we used the Luhman 16B light curves of Buenzli et al. (2015a,b) to map Luhman 16B’s TOA structure integrating over the J- and H-bands (cut at  $1.66\ \mu\text{m}$ ) of the G141 grism and in the complete G102 grism. Using multi-wavelength observations to study an ultracool atmosphere is a powerful technique that allows us to probe different layers in the observed atmosphere. Contribution functions of early T-dwarfs suggest that the J- and H-band, and the G102 grism probe very similar pressure levels (see Section 5). The maps we made using these bands thus, provide us with hints of the evolution of the atmospheric structure of Luhman 16B between the two epochs of observations.

Finally, we used the Luhman 16A curves of Buenzli et al. (2015b) to create the first map of the TOA structure of Luhman 16A. We created two maps for Luhman 16A, using the two proposed rotational rates by Buenzli et al. (2015b) and Mancini et al. (2015). Using our adapted version of *Aeolus* (see Sect. 3) we constrained the inclination of Luhman 16A for the two rotational periods.

This paper is organized as follows. In Sect. 2 we present the dataset we use in this paper. In Sect. 3 we introduce, briefly, *Aeolus*. In Sect. 4 we present the Principal component analysis results of Buenzli et al. (2015a,b). In Sects. 5 and 6 we present *Aeolus* maps of Luhman 16B and 16A respectively. Finally, in Sect. 7 we present a discussion of our results and in Sect. 8 we present our conclusions.

## 2. DATA

Luhman 16AB was observed on 2013 November 8 with HST/WFC3 with the G141 grism (from  $1.1$  to  $1.66\ \mu\text{m}$ )

TABLE 1  
SUMMARY OF OBSERVATIONS USED IN THIS PAPER.

Original Paper	Epoch	Date of observations	Band
Buenzli et al. (2015a)	1	2013 Nov. 8	J
Buenzli et al. (2015a)	1	2013 Nov. 8	H
Buenzli et al. (2015b)	2	2014 Nov. 23	G102

by Buenzli et al. (2015a), and on 2014 November 23 with HST/WFC3 with the G102 grism (from  $0.8$  to  $1.15\ \mu\text{m}$ ) by Buenzli et al. (2015b). For a detailed description of the observations and data reduction we refer the reader to Buenzli et al. (2015a,b). Each set of observations covered approximately 1.5 rotations of Luhman 16B. In Table 1 we summarize the observations we used in this paper.

Fig. 1 shows the Luhman 16 B light curves derived by integrating counts of Buenzli et al. (2015a) in the J- (red blocks) and H- (green triangles) bands (top panel), and of Buenzli et al. (2015b) over the complete G102 grism (orange triangles, bottom panel). We note that Luhman 16B has a very rapidly evolving atmosphere, and we can detect evolution in the light curves from the first to the second rotation on the 2013 observations, and from the 2013, J- and H-band light curves to the 2014 G102 light curve.

Finally, Fig. 2 shows the Luhman 16A curves derived by integrating counts over the complete G102 grism (Buenzli et al. 2015b), assuming a rotational period of 8 hr (grey blocks) and 5 hr (orange stars). The J-band (magenta triangles) light curve from Buenzli et al. (2015a) is also plotted for comparison.

## 3. AEOLUS

We mapped Luhman 16B using *Aeolus*. *Aeolus* is an MCMC code that combines a Gibbs sampler with a random-walk Metropolis-within-Gibbs algorithm to map the TOA (per observational wavelength) structure of ultracool atmospheres (Karalidi et al. 2015). *Aeolus* assumes that variations in the observed light curves are due to elliptical, spot-like features (see, Karalidi et al. 2015) and fits the number of spots as a free parameter. For every spot, *Aeolus* fits the position (longitude and latitude), angular size, and contrast ratio to the background TOA.

In this paper we allowed the contrast ratio of every spot to the background to vary between 0.01 and 2.0, and set the maximum allowed number of spots to 7. We varied *Aeolus* in comparison to (Karalidi et al. 2015) to fit the inclination and limb darkening of our target as extra free parameters. As discussed in Karalidi et al. (2015), since there is no intrinsic reason why *Aeolus* should prefer specific values of the parameters it fits (longitude, latitude, size and contrast ratio) over others, we assign a uniform prior ( $p(x) \sim 1$ ) over their respective parameter ranges. We assume that the observational errors are nearly Gaussian, with known variances, and adopt a normal likelihood distribution ( $p(d|x) \sim \exp[-\chi^2(x)/2]$ ).

For every light curve we ran eight chains of 5,000,000 steps each. Removal of possible biases rising from our selection of initial conditions was done by removing the first 500,000 steps (10%) of the chains (see Karalidi et al. 2015, and references therein). The choice of the best fitting model finally took into account the minimization of the Bayesian Information Criterion (BIC) (Schwarz

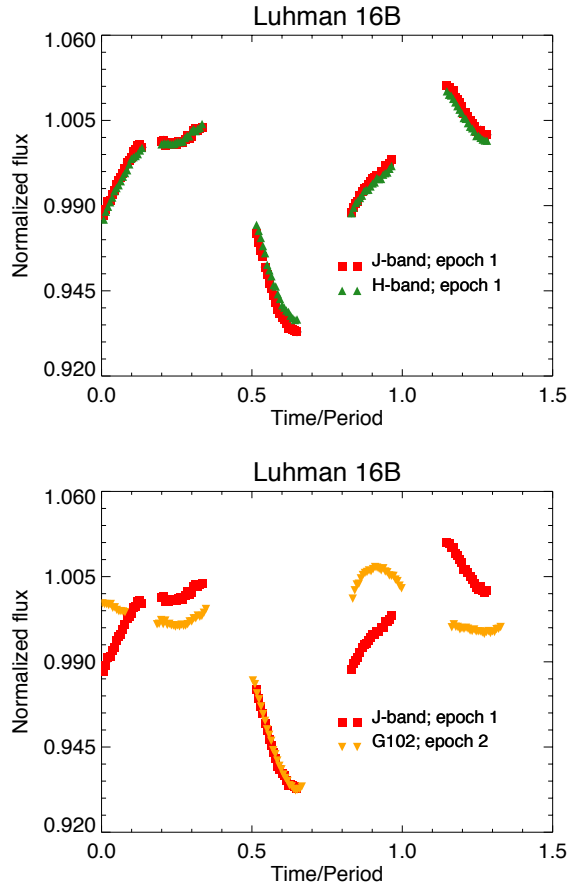


FIG. 1.— Luhman 16B light curves from Buenzli et al. (2015a) and Buenzli et al. (2015b), assuming a rotational period of 5.05 hr (Burgasser et al. 2014). Top panel: 2013 November 8, HST/WFC3 light curves in the J- (red blocks) and H- (green triangles) bands. Bottom panel: 2014 November 23, HST/WFC3, G102 light curves over the complete G102 grism (orange arrows). The J-band (red blocks) light curve is also plotted for comparison, shifted so that the trough around a rotational phase of 0.6 match.

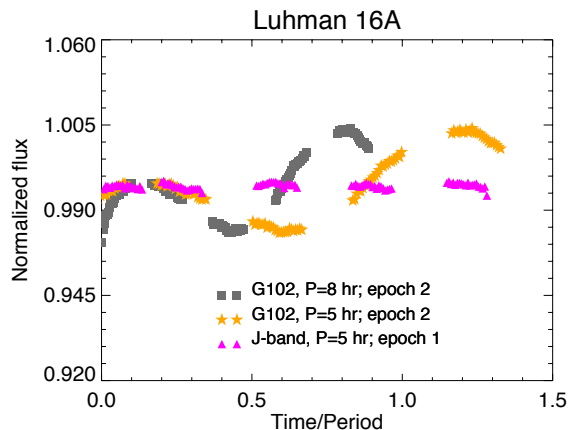


FIG. 2.— Luhman 16A HST/WFC3, G102 light curve from Buenzli et al. (2015b) (epoch 2) assuming a rotational period of 8 hr (grey blocks) and 5 hr (orange stars). The J-band (magenta triangles) light curve from Buenzli et al. (2015a) (epoch 1) is over-plotted for comparison.

1978). When comparing two models the one with the smaller BIC is preferred. If the BIC of the two models is the same, the model with the fewer free parameters is preferred. As in Karalidi et al. (2015), to control that the solution on which our MCMC chains converged did not depend on our initial guesses, we used different initial condition for each chain and used the Gelman & Rubin  $\hat{R}$  criterion to control the convergence of the chains (Gelman & Rubin 1992). To accept a solution we checked that  $\hat{R}$  is always less than 1.2. Finally, we kept our sample size  $N$  larger than the number of our fitted parameters  $\kappa$  ( $200 \gtrsim N/\kappa \gtrsim 40$ ). For a detailed description of *Aeolus* we refer the reader to Karalidi et al. (2015).

#### 4. SINGLE SPOT-COMPONENT MODEL

Buenzli et al. (2015a,b) performed a Principal Component Analysis (PCA) on their data to determine the minimum number of independent spectral components necessary to reproduce their observed spectra. They concluded that for both sets of observations the observed spectral variability could be mostly characterized by a single component, implying that only two significant discrete photospheric structures (a “background” and a “heterogeneity”) defined the TOA structure of these brown dwarfs. A similar conclusion was reached for 2MASSJ21392676+0220226 and 2MASSJ0136565+093347 by Apai et al. (2013).

We assumed that the “heterogeneity” component of the TOA is structured in the shape of elliptical, spot-like features (see Sect. 3). We then assumed that the fact that all possible spots are dominated by one spectral component implies that their temperature difference to the background TOA was similar. Assuming that any brightness variations mapped by *Aeolus* are due to the different temperatures of the areas observed, this implied that the contrast ratios of all the spots retrieved by *Aeolus* should be similar. We thus adapted *Aeolus* to keep the contrast ratio of all (possible) spots the same.

#### 5. LUHMAN 16B

We initially applied *Aeolus* on the Luhman 16B light curves of Fig. 1. These light curves cover approximately 1.3 to 1.4 rotations of Luhman 16B. The atmosphere of Luhman 16B appears to be highly active, causing the light curves to evolve already within one complete rotation (see, e.g., the change of the light curve shape between a rotational phase of 0.1 to 0.3 and 1.1 to 1.3 on the top panel of Fig. 1). For this reason we split the light curves and fitted only the first complete rotation (rotational phase 0. to 1.).

Here we present the maps *Aeolus* derived for the two epochs. We followed Karalidi et al. (2015), and assumed that brightness variations across the TOA are due to the different temperature of the areas observed. We thus used the retrieved contrast ratios to calculate brightness temperature variations across the TOA.

*Aeolus* retrieved an inclination of  $26^\circ \pm 8^\circ$  for Luhman 16B, in agreement with Crossfield et al. (2014) observations that suggested an inclination  $i < 30^\circ$ .

##### 5.1. First epoch maps

Fig. 3 (top four panels) shows the brightness temperature map of Luhman 16B in the J-band. *Aeolus* retrieved three spots (BIC~25.9 vs 41.4 for two spots)

with (longitude, latitude) =  $(113.47^\circ \pm 6.46^\circ, 31^\circ \pm 6^\circ)$ ,  $(186.08^\circ \pm 3.65^\circ, 45^\circ \pm 12^\circ)$  and  $(283^\circ \pm 13^\circ, 72^\circ \pm 10^\circ)$  and respective sizes of  $38.89^\circ \pm 0.80^\circ$ ,  $24.45^\circ \pm 1.46^\circ$  and  $35.54^\circ \pm 1.67^\circ$ . Assuming a background TOA temperature of 1280 K (Faherty et al. 2014), the retrieved spots had a temperature difference to the background TOA  $\Delta T \sim 231 \pm 16$  K.

In Fig. 4 (top panel) we show the normalized J-band light curve (stars) with error bars and the best-fit *Aeolus* curve (black line). In Fig. 4 (bottom panel) we show the corresponding residuals. The best-fit 2-spots *Aeolus* curve (red dashed-dotted line) is also shown for comparison. In Fig. 5 we show sample posterior distributions for the longitude of spot 3, the inclination of Luhman 16B (based on the J-band light curve) and the inclination of Luhman 16A assuming a rotational period of 5 hr.

To control the robustness of our results, and to take advantage of the complete light curve, we applied again *Aeolus* on the J-band light curve between a rotational phase of 0.2 to  $\sim 1.2$ . For a direct comparison with the previous fit, we present the longitudes shifted by  $\sim 70^\circ$  (rotational phase of 0.2). *Aeolus* retrieved three spots (BIC $\sim 60$  vs 71 for two spots) with (longitude, latitude) =  $(192^\circ \pm 12^\circ, 30^\circ \pm 15^\circ)$ ,  $(287^\circ \pm 12^\circ, 60^\circ \pm 12^\circ)$  and  $(376^\circ \pm 8^\circ, -10^\circ \pm 13^\circ)$ , and respective sizes of  $26^\circ \pm 1^\circ$ ,  $37^\circ \pm 1^\circ$  and  $15.5^\circ \pm 1.4^\circ$ . The properties of the first two spots were in agreement with two spots of the previous fit. The third spot *Aeolus* retrieved did not match the properties of the “first spot” of the previous fit (with longitude of  $113.47^\circ \pm 6.46^\circ$ ), hinting to the rapid evolution of the TOA structure of Luhman 16B.

Fig. 3 (bottom four panels) shows the brightness temperature map of Luhman 16B in the H-band. *Aeolus* retrieved three spots (BIC $\sim 24$  vs 42 for four spots) with (longitude, latitude) =  $(107.27^\circ \pm 5.48^\circ, 28^\circ \pm 8^\circ)$ ,  $(190.91^\circ \pm 4.83^\circ, 50^\circ \pm 20^\circ)$  and  $(288.6^\circ \pm 9.4^\circ, 74^\circ \pm 6^\circ)$  and respective sizes of  $32.42^\circ \pm 0.80^\circ$ ,  $25.02^\circ \pm 1.13^\circ$  and  $36.30^\circ \pm 1.18^\circ$ . Assuming a background TOA temperature of 1280 K, the retrieved spots had a  $\Delta T \sim 211 \pm 16$  K to the background TOA.

### 5.2. Second epoch map

Fig. 6 shows the brightness temperature map of Luhman 16B in the G102 grism. *Aeolus* retrieved 4 spots (BIC 45 vs 61.7 for three spots) with (longitude, latitude) =  $(87^\circ \pm 7^\circ, 0^\circ \pm 20^\circ)$ ,  $(154^\circ \pm 18^\circ, 28^\circ \pm 12^\circ)$ ,  $(233^\circ \pm 16^\circ, 40^\circ \pm 12^\circ)$  and  $(355^\circ \pm 15^\circ, 63^\circ \pm 8^\circ)$  and respective sizes of  $37.63^\circ \pm 0.92^\circ$ ,  $39.56^\circ \pm 1.89^\circ$ ,  $35.87^\circ \pm 2.10^\circ$  and  $13.11^\circ \pm 0.89^\circ$ . Assuming a background TOA temperature of 1280 K, the retrieved spots had a  $\Delta T \sim 119 \pm 6$  K to the background TOA.

In Table 2 we summarize the corresponding number of spots of the maps *Aeolus* retrieved. For a direct comparison of the retrieved maps Fig. 7 shows the 2013 J- (top panel) and H- (middle panel) maps, and the 2014 G102 map (bottom panel) in an equirectangular projection.

Note that the temperature differences retrieved for the spots in both epochs are comparable to the 200–300 K temperature difference reported between the best-fit models of Buenzli et al. (2015a,b), and to the  $T_{\text{hot}} - T_{\text{cold}}$  brightness temperature difference reported by Burgasser et al. (2014). These temperature differences are also comparable to the temperature difference Apai et al. (2013) retrieved for the spots

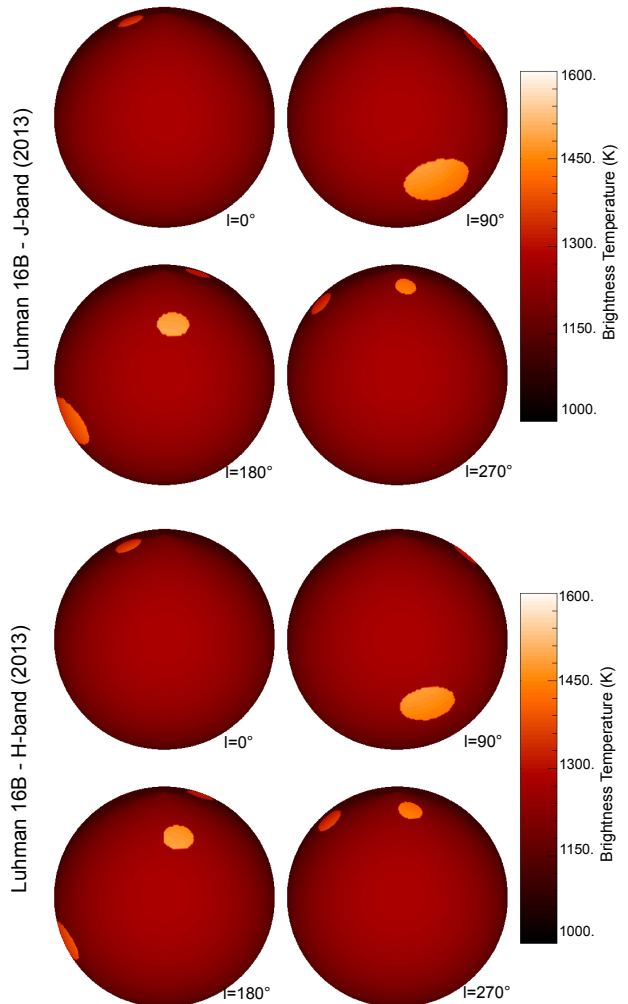


FIG. 3.— Luhman 16B brightness temperature maps from applying *Aeolus* on the J- (top four panels) and the H-band (bottom four panels) light curves of Fig. 1. The maps are centered at  $0^\circ$  of longitude (upper left map),  $90^\circ$  of longitude (upper right map),  $180^\circ$  of longitude (lower left map) and  $270^\circ$  of longitude (lower right map).

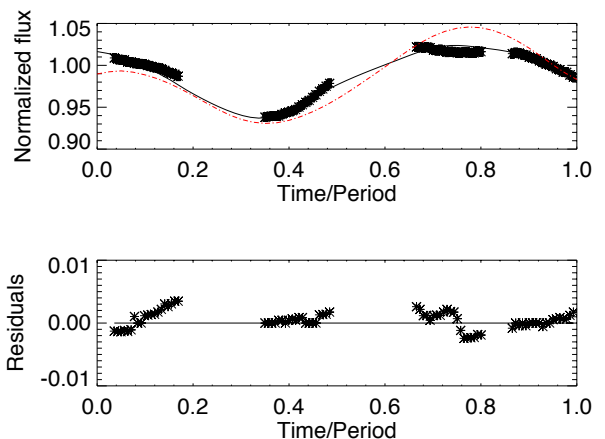


FIG. 4.— Top panel: Normalized J-band light curve of Luhman 16B (stars) with error bars and best fit *Aeolus* curve (black solid line). Note that the error bars are smaller than the symbols. Also plotted is the best fit 2-spot model (red dashed-dotted line) for comparison. Bottom panel: corresponding residuals.

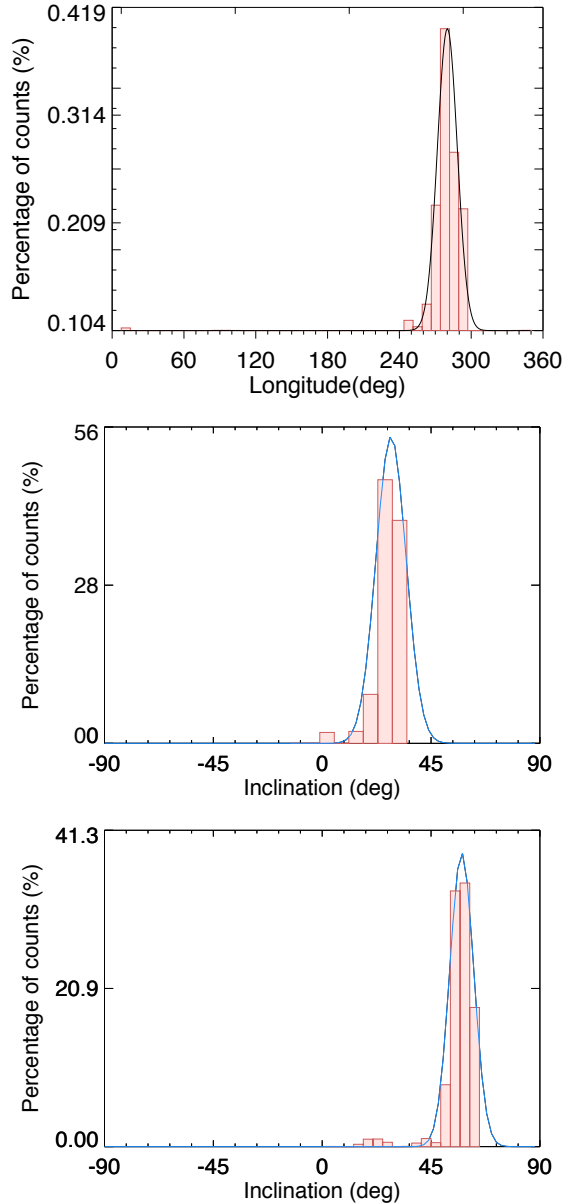


FIG. 5.— Top panel: Sample posterior distribution for the longitude of spot 3 of Luhman 16B (J-band). Middle panel: Sample posterior distribution for the inclination of Luhman 16B (J-band). Bottom panel: Sample posterior distribution for the inclination of Luhman 16A ( $P = 5$  hr).

TABLE 2  
NUMBER OF SPOTS OF THE CORRESPONDING MAPS *Aeolus* RETRIEVED FOR THE TOA OF LUHMAN 16B PER OBSERVATIONAL BAND AND EPOCH.

Epoch	Band	Number of spots
1	J	3
1	H	3
2	G102	4

on two other brown dwarfs in the L/T transition SIMP0136 and 2M2139 (2MASSJ0136565+093347 and 2MASSJ21392676+0220226 respectively).

## 6. LUHMAN 16A

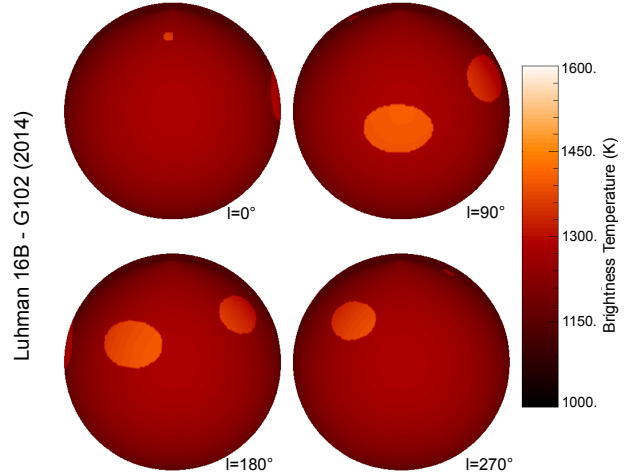


FIG. 6.— Same as Fig. 3, but using the G102 grism light curve.

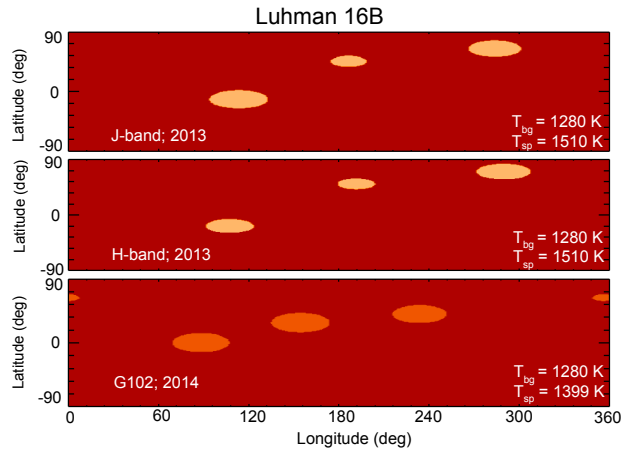


FIG. 7.— Luhman 16B maps, in an equirectangular projection, based on the J-band (top panel) and H-band (middle panel) light curves on 2013, and the G102 grism light curve on 2014 (bottom panel). The assumed background TOA brightness temperature ( $T_{bg}$ ) and the retrieved brightness temperature of the spots ( $T_{sp}$ ) is shown in every panel.

Buenzli et al. (2015b) observed variability in the atmosphere of Luhman 16A, with its rotational light curve showing a peak-to-peak amplitude of  $\sim 4.5\%$  (see bottom panel of Fig. 1), allowing us to map Luhman 16A with *Aeolus*.

We initially assumed a rotational period of 5 hr, following Buenzli et al. (2015b). As discussed in Crossfield et al. (2014), a similar rotational period for Luhman 16B and 16A would imply that the two brown dwarfs' rotational axes are misaligned. *Aeolus* retrieved an inclination of  $56^\circ \pm 5^\circ$ .

Fig. 8 (top four panels) shows the brightness temperature map of Luhman 16A assuming a rotational period of 5 hr. *Aeolus* retrieved three spots ( $BIC \sim 24.2$  vs 37.5 for two spots) with (longitude, latitude) =  $(115^\circ \pm 8^\circ, 32^\circ \pm 10^\circ)$ ,  $(0^\circ \pm 8^\circ, 43^\circ \pm 8^\circ)$  and  $(287^\circ \pm 18^\circ, 74^\circ \pm 10^\circ)$  and respective sizes of  $37.72^\circ \pm 6.96^\circ$ ,  $35.65^\circ \pm 1.10^\circ$  and  $36.34^\circ \pm 1.21^\circ$ . Assuming a background TOA temperature of 1310 K (Faherty et al. 2014), the retrieved spots had a temperature difference to the background TOA of  $216 \pm 5$  K. In Fig. 9 we show the normalized G102 light

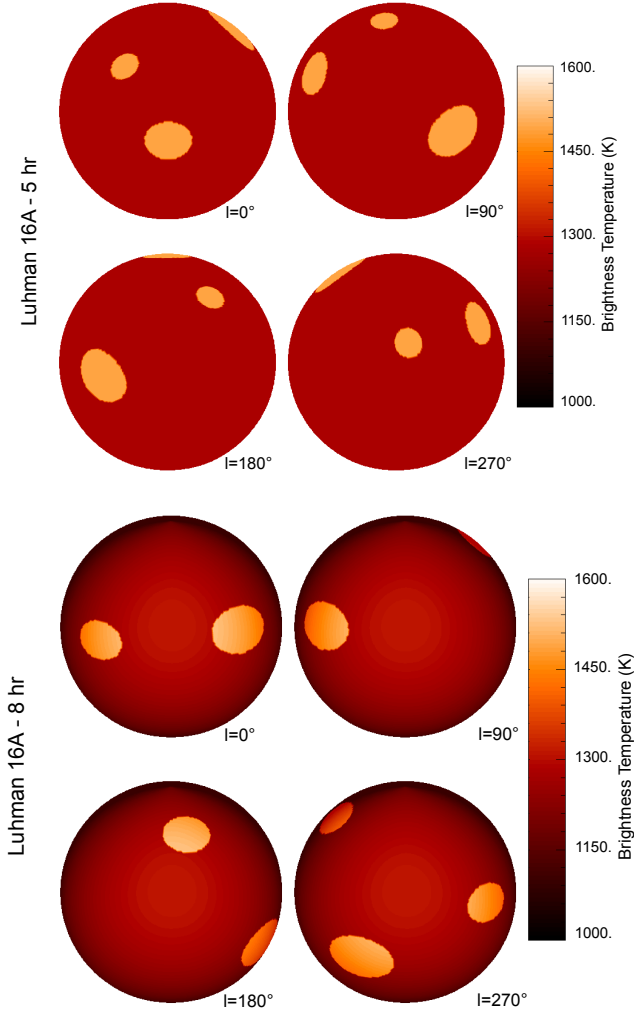


FIG. 8.— Luhman 16A brightness temperature maps from applying *Aeolus* on the HST/WFC3, G102 light curves of Fig. 1 (bottom panel), assuming a rotational period of 5 hr (top four panels), or 8 hr (top four panels). The maps are centered at  $0^\circ$  of longitude (upper left map),  $90^\circ$  of longitude (upper right map),  $180^\circ$  of longitude (lower left map) and  $270^\circ$  of longitude (lower right map).

curve of Luhman 16A (stars) with error bars and the best-fit *Aeolus* curve (top panel), and the corresponding residuals (middle panel).

We then assumed a rotational period of 8 hr, following Mancini et al. (2015). Mancini et al. (2015) performed spatially resolved, ground-based observations of Luhman 16AB over sixteen consecutive nights to estimate the rotational period of both components. Using a Gaussian process model and a MCMC analysis they retrieved a preferred period of 8 hr for Luhman 16A. However, they noted that a wide range of rotational periods are consistent with their data. *Aeolus* retrieved an inclination of  $18^\circ \pm 8^\circ$ , in agreement with the retrieved Luhman 16B inclination. As discussed in Crossfield et al. (2014), a different rotational period for Luhman 16A and B would allow the rotational axes of the two brown dwarfs to be aligned, as *Aeolus* retrieved.

Fig. 8 (bottom four panels) shows the brightness temperature map of Luhman 16A assuming a rotational period of 8 hr. *Aeolus* retrieved four spots (BIC $\sim$ 21.6 vs 31.8 for three spots) with (longitude, latitude) =

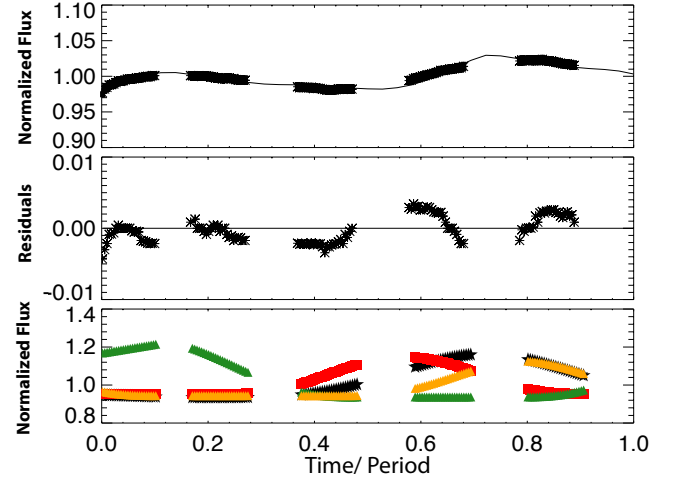


FIG. 9.— Top panel: Normalized G102 light curve of Luhman 16A with a 8 hr rotational period (stars), with error bars and best fit *Aeolus* curve (black solid line). Note that the error bars are smaller than the symbols. Middle panel: corresponding residuals. Bottom panel: Normalized light curves showing the contribution of each one of the four spots for our best-fit model.

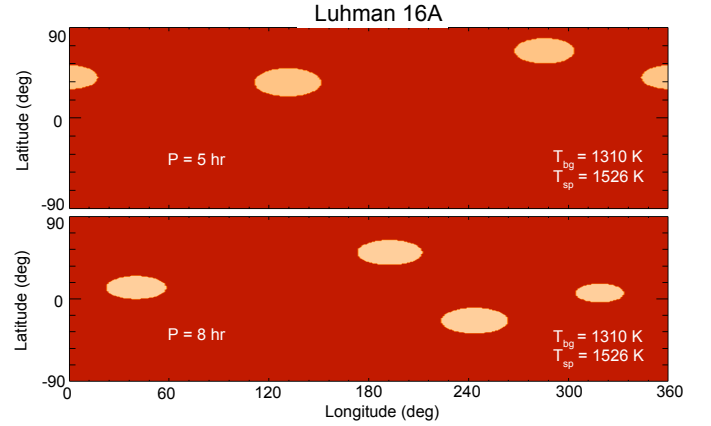


FIG. 10.— Luhman 16A maps assuming a rotational period of 5 hr (top panel), or 8 hr (bottom panel).

$(191.92^\circ \pm 16.23^\circ, 50^\circ \pm 8^\circ)$ ,  $(243^\circ \pm 10^\circ, -24^\circ \pm 10^\circ)$ ,  $(318^\circ \pm 20^\circ, 6^\circ \pm 20^\circ)$  and  $(40^\circ \pm 6^\circ, 12^\circ \pm 20^\circ)$  and respective sizes of  $38.67^\circ \pm 0.57^\circ$ ,  $39.44^\circ \pm 1.63^\circ$ ,  $28.88^\circ \pm 1.16^\circ$  and  $36.37^\circ \pm 1.23^\circ$ . Assuming a background TOA temperature of 1310 K (Faherty et al. 2014), the retrieved spots had a temperature difference to the background TOA of  $238 \pm 10$  K. Table 3 summarizes the properties of all spots *Aeolus* retrieved at the TOA of Luhman 16A and B, per observational band and epoch.

## 7. DISCUSSION

### 7.1. Comparison of *Aeolus* map with previously published Luhman 16B map.

Crossfield et al. (2014) mapped Luhman 16B using Doppler imaging and found a complex map, with both brighter and darker than the background TOA cloud patches (see bottom panel of Fig. 11). This contradicts the PCA analysis of Buenzli et al. (2015a,b) that found that only one kind of cloud patches/spots is necessary to explain the variability of the observed spectra. Given the



TABLE 3  
PROPERTIES OF THE SPOTS *Aeolus* RETRIEVED AT THE TOA OF LUHMAN 16A AND B PER OBSERVATIONAL BAND AND EPOCH.

Target	Period (hr)	Epoch	Band	Longitude	Latitude	Size	Temperature Contrast
Luhman 16A	5	2	G102	$115^\circ \pm 8^\circ$	$32^\circ \pm 10^\circ$	$37.72^\circ \pm 6.96^\circ$	$216 \pm 5$ K
				$0^\circ \pm 8^\circ$	$43^\circ \pm 8^\circ$	$35.65^\circ \pm 1.10^\circ$	$216 \pm 5$ K
				$287^\circ \pm 18^\circ$	$74^\circ \pm 10^\circ$	$36.34^\circ \pm 1.21^\circ$	$216 \pm 5$ K
Luhman 16A	8	2	G102	$191.92^\circ \pm 16.23^\circ$	$50^\circ \pm 8^\circ$	$38.67^\circ \pm 0.57^\circ$	$238 \pm 10$ K
				$243^\circ \pm 10^\circ$	$-24^\circ \pm 10^\circ$	$39.44^\circ \pm 1.63^\circ$	$238 \pm 10$ K
				$40^\circ \pm 6^\circ$	$12^\circ \pm 20^\circ$	$36.37^\circ \pm 1.23^\circ$	$238 \pm 10$ K
				$318^\circ \pm 20^\circ$	$6^\circ \pm 20^\circ$	$28.88^\circ \pm 1.16^\circ$	$238 \pm 10$ K
Luhman 16B	5.05	1	J	$113.47^\circ \pm 6.46^\circ$	$-20^\circ \pm 12^\circ$	$38.89^\circ \pm 0.80^\circ$	$231 \pm 16$ K
				$186.08^\circ \pm 3.65^\circ$	$45^\circ \pm 12^\circ$	$24.45^\circ \pm 1.46^\circ$	$231 \pm 16$ K
				$283^\circ \pm 13^\circ$	$72^\circ \pm 10^\circ$	$35.54^\circ \pm 1.67^\circ$	$231 \pm 16$ K
Luhman 16B	5.05	1	H	$107.27^\circ \pm 5.48^\circ$	$-18^\circ \pm 8^\circ$	$32.42^\circ \pm 0.80^\circ$	$211 \pm 16$ K
				$190.91^\circ \pm 4.83^\circ$	$51^\circ \pm 20^\circ$	$25.02^\circ \pm 1.13^\circ$	$211 \pm 16$ K
				$288.6^\circ \pm 9.4^\circ$	$74^\circ \pm 6^\circ$	$36.30^\circ \pm 1.18^\circ$	$211 \pm 16$ K
Luhman 16B	5.05	2	G102	$87^\circ \pm 7^\circ$	$0^\circ \pm 20^\circ$	$37.63^\circ \pm 0.92^\circ$	$119 \pm 6$ K
				$154^\circ \pm 18^\circ$	$28^\circ \pm 12^\circ$	$39.56^\circ \pm 1.89^\circ$	$119 \pm 6$ K
				$233^\circ \pm 16^\circ$	$40^\circ \pm 12^\circ$	$35.87^\circ \pm 2.10^\circ$	$119 \pm 6$ K
				$355^\circ \pm 15^\circ$	$63^\circ \pm 8^\circ$	$13.11^\circ \pm 0.89^\circ$	$119 \pm 6$ K

night-to-night variability of Luhman 16B's light curves one could argue that the observed difference could be due to the  $\sim 0.5$  year between the Crossfield et al. (2014) and Buenzli et al. (2015a) observations. However, the Buenzli et al. (2015a) and Buenzli et al. (2015b) observations were taken  $\sim 1$  year apart and the PCA analysis of the two datasets were in agreement. Crossfield et al. (2014) observed Luhman 16B in the CO absorption lines in the K-band, probing lower pressure levels in the Luhman 16B atmosphere than the G141 and G102 grism observations of Buenzli et al. (2015a,b) ( $\sim 0.94$  bar versus  $\sim 2.7$  bar, see Fig. 12). The different pressure levels probed could explain the difference between the mixed-spot map of Crossfield et al. (2014) and the single-temperature-spot maps implied by the PCA analysis of Buenzli et al. (2015a,b). However, this could imply that different mechanisms rule the formation of spots in the deeper and upper atmosphere (blocking or allowing the formation of brighter and darker spots, respectively). Note that in a Doppler imaging map brighter/darker spots could also be caused by variations in the atmospheric abundances across the TOA. Assuming that some of these features could indicate abundance variations, rather than cloud, heterogeneities could explain the difference between the PCA analysis and the Crossfield et al. (2014) mixed-spot map. However, HST spectral mapping by Buenzli et al. (2015a,b) showed no evidence for abundance variations in the G102 and G141 grism.

For a direct comparison of our maps with the Crossfield et al. (2014) map (hereafter C14 map) we again applied *Aeolus* on the J-band light curve of Fig. 1, this time allowing *Aeolus* to fit the contrast ratio of every spot independently of the others. *Aeolus* retrieved four spots (BIC $\sim 38.9$ ) with (longitude, latitude) = ( $84.72^\circ \pm 8.83^\circ$ ,  $23^\circ \pm 8^\circ$ ), ( $155.87^\circ \pm 8.47^\circ$ ,  $42^\circ \pm 9^\circ$ ), ( $227.3^\circ \pm 8.7^\circ$ ,  $59^\circ \pm 6^\circ$ ) and ( $301.28^\circ \pm 8.08^\circ$ ,  $30^\circ \pm 11^\circ$ ) and respective sizes of  $31.99^\circ \pm 1.19^\circ$ ,  $20.87^\circ \pm 1.12^\circ$ ,  $28.85^\circ \pm 1.16^\circ$  and  $36.92^\circ \pm 1.14^\circ$ . Assuming a background TOA temperature of 1280 K, the retrieved spots had a  $\Delta T \sim -23 \pm 6$  K,  $38 \pm 6$  K,  $141 \pm 6$  K and  $-51 \pm 6$  K to the background TOA. Note that the multiple-component model has a larger BIC than our single-component model ( $\sim 39$  vs  $\sim 26$ ), so the latter would be preferred (by *Aeolus*) over the former.

Fig. 11 (top and middle panels) shows the brightness temperature maps of Luhman 16B allowing *Aeolus* to fit the contrast ratio of all (possible) spots independently of the others. The Doppler imaging map of Crossfield et al. (2014) is also shown for comparison (bottom panel). As in Crossfield et al. (2014), *Aeolus* found a mixture of darker and brighter than the background TOA spots. We compared the spots *Aeolus* retrieved with the highest signal-to-noise-ratio features of the C14 map (see Fig. 11). Note though, that the  $\sim 0.5$  year between the Crossfield et al. (2014) and Buenzli et al. (2015a) observations, in combination with the observed night-to-night evolution of Luhman 16B's light curves (and thus TOA structure), indicates that, probably, our maps probed very different features from the C14 map.

An interesting result is that *Aeolus* retrieved a very large, dark spot (the largest, and darkest spot in the *Aeolus* map) in agreement with the C14 map, even though the latter map probed higher altitudes in the atmosphere ( $\sim 0.94$  bar versus  $\sim 2.7$  bar of our map). Both the *Aeolus*' and the C14 map's darkest spots lay at low latitudes. The spot *Aeolus* retrieved was  $\sim 51$  K cooler than the background TOA and spanned  $\sim 37^\circ$  of longitude, while the spot of the C14 map was  $\sim 40$  K cooler than the background TOA (assuming a background temperature of  $\sim 1450$  as in Crossfield et al. (2014)) and spanned  $\sim 42^\circ - 48^\circ$  of longitude. The brightest spot *Aeolus* retrieved was  $\sim 141$  K hotter than the background TOA and lay at mid latitudes, while the brightest spot of the C14 map was  $\sim 26$  K hotter than the background TOA and lay at high latitudes. Finally, the brightest and darkest spots *Aeolus* retrieved lay  $\sim 74^\circ$  of longitude apart, while the brightest and darkest spots of the C14 map lay  $\sim 190^\circ$  of longitude apart.

A notable difference between the *Aeolus* and the C14 maps is that the latter contains latitudinally extensive cloud patches, while the former contains narrower spots. The latitudinal extensive patches are intrinsic to the Doppler imaging maps, since they appear even when the input maps contain latitudinally narrow spots (compare, e.g., the input map and the retrieved maps of Unruh & Collier Cameron (1995), or the input and retrieved maps of Crossfield et al. (2014) [their Fig. 5]). The latitudinal

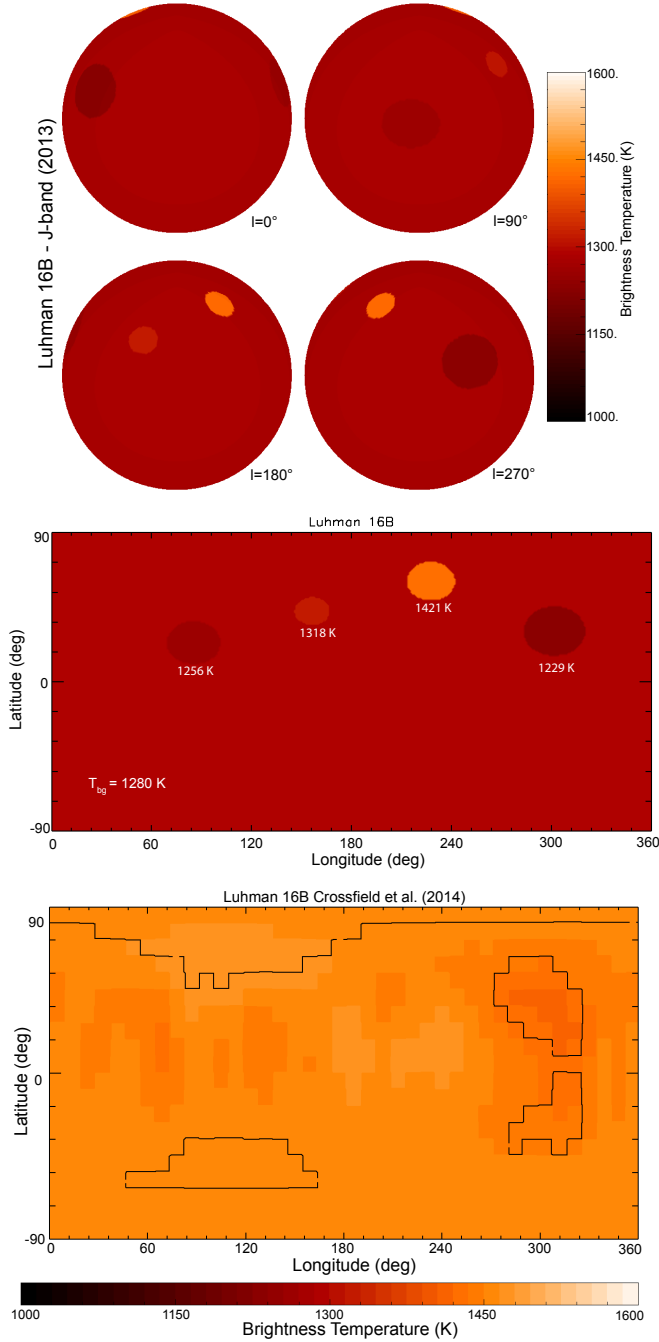


FIG. 11.— Top panel: Same as in Fig. 3 (top panels), but allowing *Aeolus* to fit the brightness temperature (i.e., contrast ratio) of every spot independently of the others. Middle panel: Same map as top panel, but in an equirectangular projection. Bottom panel: Crossfield et al. (2014) map in an equirectangular projection. Black contour lines show the features with the highest signal-to-noise ratio ( $\geq 3$ ): a polar, brighter than the background TOA spot and a mid-latitude, darker than the background TOA spot.

extensive cloud patches of the C14 maps thus, do not contradict *Aeolus*' latitudinally narrower spots.

Another difference between the C14 and the *Aeolus* maps is that the former shows more features than the latter. In Karalidi et al. (2015) we showed that *Aeolus* could not detect small scale features of the TOA ( $\lesssim 10^\circ$ ). However, most of the features in the C14 map are extensive enough for *Aeolus* to have mapped them. Most of the

features in the C14 map have a very low signal-to-noise-ratio making their detection ambiguous. Some of these features could be artifacts of the Doppler imaging due to, e.g., a slightly offset assumed limb darkening or inclination (see, e.g., Vogt et al. 1987; Unruh & Collier Cameron 1995). Additionally, given that Doppler imaging is also sensitive to abundance variations across the atmosphere, these features could indicate abundance, rather than cloud, heterogeneities. Finally, note again that the time elapsed between the two observations (Crossfield et al. (2014) and Buenzli et al. (2015a)) indicates that, probably, our maps probed very different features from the C14 map.

## 7.2. Implications of *Aeolus* maps for the atmospheres of Luhman 16A & B.

### 7.2.1. Wind speeds and characteristic timescales.

Assuming that the maximum spot size retrieved by *Aeolus* is defined by the atmospheric jet size, we can follow a Rhines-length-based argument as in Apai et al. (2013); Burgasser et al. (2014) and Karalidi et al. (2015) to constrain the wind speed on Luhman 16A and B. We assume that our maps are accurate, and that the retrieved spots in the TOA are uniform. We additionally assume that Luhman 16A's and B's radii are equal to one Jupiter radius (evolutionary models suggest that the radius of Luhman 16B, assuming an age between 0.5 Gyr and 5 Gyr, is  $\sim 1.0 \pm 0.2 R_{\text{Jup}}$ , see Saumon & Marley (2008); Burrows et al. (2011)) and we use the maximum spot size *Aeolus* retrieved to calculate the wind speed in the atmospheres of Luhman 16A and B as:  $u_{\text{wind}} \sim \Omega R / s^2$ , where  $\Omega$  is the angular velocity,  $R = 1 \times R_{\text{Jup}}$  and  $s$  is the maximum spot size. For Luhman 16A this implies a wind speed  $u_{\text{wind}} \sim 602 \pm 49$  or  $891 \pm 58$  m/s, depending on the assumed rotation rate (8 hr or 5 hr, and assuming a  $\delta p \sim 0.1$  hr similar to Luhman 16B), while for Luhman 16B this implies a  $u_{\text{wind}} \sim 813 \pm 55$  m/s ( $934 \pm 37$  m/s) based on the H- (J-) band map, and  $\sim 968 \pm 94$  m/s based on the G102 map. These speeds are higher than the wind speeds of the giant planets of our Solar system, but are lower, or comparable to the wind speeds reported for highly irradiated hot Jupiters by, e.g., Louden & Wheatley (2015); Colón et al. (2012) and Snellen et al. (2010). Previous calculations of the wind speed on Luhman 16B by Burgasser et al. (2014) predicted wind speeds between 1600 m/sec and 3400 m/sec, assuming a background TOA temperature of 1510K and a spot-temperature of  $1700\text{K} < T < 1900\text{K}$ . These speeds are higher than the ones *Aeolus* retrieved. However, since these speeds are upper limits our results do not contradict, but rather further constrain the results of Burgasser et al. (2014).

We performed a back-of-the-envelope calculation of the speed of sound,  $c_s$ , on Luhman 16A and B.  $\text{H}_2$  is the major constituent of both brown dwarfs' and Jupiter's atmospheres. We took thus into account the variation of the specific heat ratio of  $\text{H}_2$  between Jupiter's  $\sim 165$  K and Luhman 16A and B  $\sim 1300$  K, as well as the variation between these atmospheres' relative molecular mass. Assuming that  $c_{s-\text{Jupiter}} \sim 1,000$  m/sec at 1.5 bar (Lorenz 1998), we found that in Luhman 16A and B  $c_s \sim 2800$  m/sec. This implies that the wind speeds we retrieved using *Aeolus* and a Rhines-length-based argument are subsonic, and thus plausible for Luhman 16A and B at



mospheres.

Using the retrieved wind and sound speeds for the atmospheres of Luhman 16A and B we calculated the minimum timescales associated with wind- and density-wave- driven changes in these atmospheres. Assuming that Luhman 16A's and B's radii are equal to Jupiter's radius and setting  $t_s \sim R/c_s$  we find  $t_s \sim 6.94$  hr, i.e.,  $\sim 1.37$  Luhman 16B rotations and  $\sim 1.37$  or  $\sim 0.87$  Luhman 16A rotations, depending on the assumed rotational period (5 hr or 8 hr respectively). The advection timescale  $t_w \sim R/u_{\text{wind}}$  of Luhman 16A's atmosphere is  $t_w \sim 32.26$  hr (23.65 hr) or 4 (4.68) Luhman 16A rotations, depending on the assumed rotational period. For Luhman 16B  $t_w \sim 23.89$  hr (20.79 hr, or 20.06 hr) or 4.7 (4.12, or 3.97) rotations based on the H-band (J-band, or G102 grism) map. If we define a timescale  $t_h$  as the time required for a spot to be horizontally displaced by a full spot-sized length ( $\sim 40^\circ$  or  $\sim 0.7R$ ) due to the atmospheric wind, we get:  $t_h \sim 22.6$  hr (16.6 hr) or 2.8 (3.3) Luhman 16A rotations, and  $t_h \sim 16.7$  hr (14.6 hr, or 14 hr) or 3.3 (2.9, or 2.8) Luhman 16B rotations. Space and ground-based observations of Luhman 16B show evolution of its light curve within a couple of rotations, indicating that the TOA structure of Luhman 16B changes in timescales of 1–5 rotations (see, e.g., Buenzli et al. (2015a,b); Mancini et al. (2015)). This is comparable to the timescales we inferred here for density-wave- and horizontal wind- driven changes in the atmosphere of Luhman 16B.

#### 7.2.2. Luhman 16B's evolving cloud structures.

Apai et al. (2013) and Buenzli et al. (2014, 2015a) showed that the observed variability of light curves of brown dwarfs in the L/T transition is not caused by cloud clearings, but by variations in the optical thickness of clouds across the TOA. A similar behavior is observed for the giant, cloud covered, planets of our Solar System. For example, Karalidi et al. (2015) showed that the disk-integrated light curves of Jupiter in the F275W and F763M are comparable to observed light curves of brown dwarfs, and are dominated by two distinct cloud features: the Great Red Spot (a towering cloud structure in the Jovian atmosphere) and a major  $5 \mu\text{m}$  Hot Spot (a region of thinner clouds that allows us to see deeper cloud layers in the Jovian atmosphere). Recently, Simon et al. (2015) acquired K2 observations of Neptune over 49 days and showed that the disk-integrated light curve of Neptune is dominated by a few distinct cloud features. Using the K2 observations in combination with Hubble Space Telescope and Keck imaging Simon et al. (2015) proposed that a combination of stable, large-scale cloud features and smaller, short-lived cloud features defines the TOA structure and the observed light curve variability. A similar combination could be responsible for the observed variability in brown dwarf light curves. The best-fit maps of *Aeolus* for Luhman 16A and B have spots that are hotter than the background TOA. This could be, for example, the case when due to thinner clouds we see deeper, hotter layers of the atmosphere. These areas of thinner clouds could be caused by convective downdrafts, in a similar way that Jupiter's  $5 \mu\text{m}$  Hot Spots are thought to be formed (see, Showman & Ingersoll 1998; Showman & Dowling 2000).

Using the contribution function of a T2 dwarf for

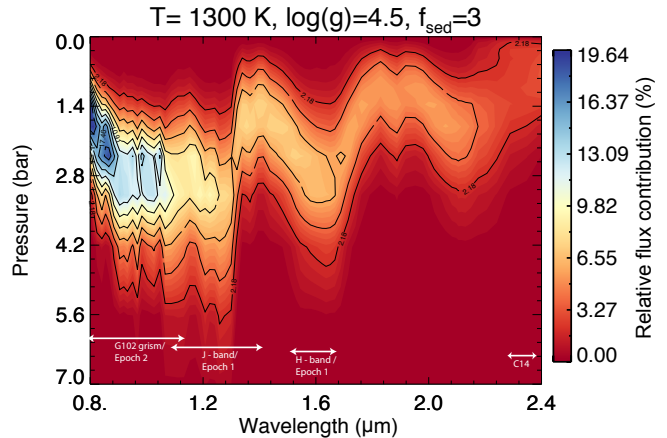


FIG. 12.— Relative flux contribution of every pressure level in the best-fit model atmosphere of Buenzli et al. (2015a) as a function of wavelength. The wavelength ranges observed in the two observational epochs used in this paper, as well as in Crossfield et al. (2014) (C14), are shown with white arrows.

Luhman 16B we note that the J-band and the G102 grism probe approximately the same pressure ranges (see Fig. 12). When comparing the maps of the two epochs one can thus deduce the evolution of the pressure layer over the  $\sim 1800$  rotations between the two observations. The maps show considerable difference between the two epochs (see Fig. 7). However, we caution that the spots of the second epoch are probably not the same as the ones of the first epoch. Luhman 16B light curves exhibit a significant evolution from one rotational period to the next. Assume that the observed evolution over the  $\sim 9,000$  hr ( $\sim 1800$  rotations) between the two observational epochs is solely due to the longitudinal shift of spots due to winds and possible appearance of new spots. If we then assume a constant wind speed of  $u_{\text{wind}} \sim 934$  m/s being responsible for the displacement of the spots of epoch 1, in epoch 2 the spots would be displaced by  $\sim 68^\circ$  of longitude. This is a  $\sim 38\%$  to  $\sim 75\%$  larger displacement than what we observe in our maps, implying that more mechanisms are responsible for our light curve evolution.

Space and ground-based observations of Luhman 16B show a rapid evolution of the observational light curves, indicating a rapidly changing atmosphere. During the  $\sim 1800$  rotations that separate the two epochs of the observations used in this paper, Luhman 16B's TOA structure should have varied multiple times. Indeed, Mancini et al. (2015) ground-based observations of Luhman 16B between 2014 April 19 and 2014 July 16 showed that Luhman 16B's light curve evolved from one night to the next (see their Fig. 6). Note that the Mancini et al. (2015) observations were made in the  $i+z$  bands, which, shortward of  $0.8 \mu\text{m}$ , probe higher altitudes of Luhman 16B's atmosphere than the G102 band.

It is interesting to estimate the TOA map of Luhman 16B between the two observational epochs of this paper using the Mancini et al. (2015) light curves (their Fig. 6, hereafter MLC). We were not interested in an accurate mapping, but rather a sketch of the TOA structure. Thus, we did not apply *Aeolus* on the MLC but instead we performed a visual comparison of the MLC with light curves *Aeolus* produced, assuming that all (possible) spots are hotter than the background TOA

by  $\sim 200$  K (see Fig. 7). The best-fit maps included three-or-more spots, whose location on the TOA varied from one light curve (night) to the next. For example a visual comparison of *Aeolus* light curves with the “MDJ-56770” light curve gives a best-fit for three spots, for the “MDJ-56775” light curve for four spots, and for the “MDJ-56778” light curve for three spots. Given that the MLC were separated by as little as  $\sim 5$  rotations from each other, the variability of our best-fit maps indicates a highly variable atmosphere. In the future, the acquisition of continuous, multi-rotation observations of Luhman 16B will be of great interest. Applying *Aeolus* on the light curves of such observations, we will be able to continuously map the variability of Luhman 16B’s TOA and provide feedback to General Circulation and Radiative Transfer models to help understand the mechanisms that rule the observed variability.

### 7.2.3. The Possible Persistent Cloud Structure PPCS-1

An inspection of the J- (or H-) band light curve of epoch 1 and the G102 grism light curve of epoch 2 showed the existence of a similar trough around a rotational phase of 0.6. The shape of these troughs was similar even though the two observational epochs were separated by  $\sim 1800$  rotations (see Fig. 1). The similarity of the troughs in these light curves hints to the existence of a similar feature in the TOA of Luhman 16B in the two epochs. We hereafter refer to this feature as: Possible Persistent Cloud Structure PPCS-1. We observed a similar trough in some of the light curves of Gillon et al. (2013) (observed in the  $I + z$  TRAPPIST filter), while none of the Mancini et al. (2015) light curves (observed in the  $i + z$  Danish 1.54m long-pass filter) contained a trough that matched the PPCS-1.

Fig. 13 shows the PPCS-1 in the two epochs of HST light curves used in this paper, and the matching PPCS-1 of Gillon et al. (2013) light curves. Note that the phase (time/period) of the light curves is altered in comparison to Fig. 1, and that we shifted the light curves so that the troughs of PPCS-1 match. The Gillon et al. (2013) observations took place  $\sim 2800$  rotations before the epoch 1, and  $\sim 4600$  rotations before the epoch 2 observations used in this paper. The existence of PPCS-1 in these five light curves separated by tens of hundreds of rotations is intriguing. Note that the Gillon et al. (2013) observations used the  $I + z$  filter of the TRAPPIST telescope, and probe higher (similar) altitude levels in the atmosphere of Luhman 16B than our G102 grism light curve shortwards (longwards) of  $\sim 0.8\mu\text{m}$ .

We performed a back-of-the-envelope calculation of the orbital period of an exoplanet responsible for PPCS-1. Taking into account the observed J-band “transit” depth and duration, and assuming a circular orbit with an impact parameter  $b = 0$  (the planet transits through the center of the Luhman 16B’s disk), we calculated an orbital period of  $\sim 101$  hr [a more accurate fit of the PPCS-1 to possible exoplanet orbits gave a best-fit for periods of  $\gtrsim 500$  days (Ben W. P. Lew, private communication)]. We thus ruled out the possibility that PPCS-1 was due to an exoplanet, since the PPCS-1 was visible in two successive Luhman 16B rotations in the Gillon et al. (2013) light curves (see the “Gillon+14, 376.6” and “Gillon+14, 376.68” PPCS-1 in Fig. 13).

Assuming the PPCS-1 is due to a TOA feature this

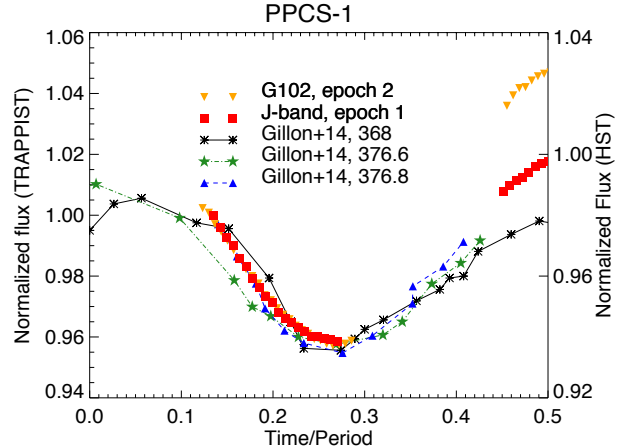


FIG. 13.— Luhman 16B light curves observed hundreds of rotations from each other exhibit a similar trough, indicating the existence of a similar feature in the TOA of Luhman 16B (PPCS-1). Note that we shifted the light curves so that the trough of PPCS-1 match.

could indicate either the existence of a stable formation (like the Great Red Spot of Jupiter) that periodically reappears at the TOA, or similar formations that appear and disappear at different times. In the case of a stable formation variations in other, unrelated cloud structures could occasionally wash out the modulations, thus explaining why the PPCS-1 is only detected in some, but not other, light curves. In the case of similar formations appearing at different observation times this could imply a possible preferred size for cloud structures in the TOA of Luhman 16B. Longer, multi-wavelength observations of Luhman 16B over (partially) continuous rotations could help clarify the nature of this feature.

## 8. CONCLUSIONS

We presented the first map of Luhman 16A and maps of two epochs of Luhman 16B. *Aeolus* constrained the inclination of Luhman 16A to  $18^\circ \pm 8^\circ$  or  $56^\circ \pm 5^\circ$ , depending on the assumed rotational period, and  $26^\circ \pm 8^\circ$  for Luhman 16B.

In agreement with the complexity of the observational light curves *Aeolus* retrieved complex top-of-the-atmosphere cloud structures for both Luhman 16A and 16B, with a surface spot coverage of 19% to 32% (depending on the assumed rotational period), and  $\sim 21\%$  (2013) to  $\sim 39\%$  (2014) respectively.

We compared our Luhman 16B maps with the only previously published map of Crossfield et al. (2014). Using the principal component analysis results of Buenzli et al. (2015a,b) *Aeolus* retrieved hotter than the background TOA spots for both observational epochs, unlike the hotter and cooler than the background TOA spots mixture that Crossfield et al. (2014) map showed. Relaxing the PCA induced constraints *Aeolus* fit a mixture of hotter and cooler (than the background TOA) spots, in agreement with the Crossfield et al. (2014) map. Interestingly, the largest spot *Aeolus* retrieved was the coolest spot and lay at low latitudes, in agreement with the Crossfield et al. (2014) map, even though the latter probed higher altitudes in the atmosphere of Luhman 16B. However, the BIC of the mixed-spot solution was larger than that of hotter-only spot solution, making the latter the preferred *Aeolus* map.

Finally, we reported the detection of a feature (PPCS-1) that reappeared in light curves of Luhman 16B that are separated by tens of hundreds of rotations from each other. We excluded the possibility that this feature is due to an exoplanet and speculated that it is related to TOA structures of Luhman 16B.

This work is part of the Spitzer Cycle-9 Exploration Program Extrasolar Storms (program No. 90063). Support for this work was provided by NASA through an award issued by JPL/Caltech. Support for Program number 12314 was provided by NASA through a grant from the Space Telescope Science Institute, which is operated by the Association of Universities for Research in Astronomy, Incorporated, under NASA contract NAS5-

26555. An allocation of computer time from the UA Research Computing High Performance Computing (HTC) and High Throughput Computing (HTC) at the University of Arizona is gratefully acknowledged. This study, in part, is based on observations made with the NASA/ESA Hubble Space Telescope, obtained at the Space Telescope Science Institute, which is operated by the Association of Universities for Research in Astronomy, Inc., under NASA contract NAS 526555. D. Apai acknowledges support by the National Aeronautics and Space Administration under Agreement No. NNX15AD94G for the program Earths in Other Solar Systems. We thank I.J.M. Crossfield for providing us with the previously published Luhman 16B map dataset. We thank Ben W. P. Lew for providing us with a best-fit exoplanet period for the PPCS-1 in Luhman 16B light curves. We thank the anonymous referee for a helpful report.

## REFERENCES

- Apai, D., Radigan, J., Buenzli, E., Burrows, A., Reid, I. N., & Jayawardhana, R. 2013, *ApJ*, 768, 121
- Biller, B. A., Crossfield, I. J. M., Mancini, L., Ciceri, S., Southworth, J., Kopytova, T. G., Bonnefoy, M., Deacon, N. R., Schlieder, J. E., Buenzli, E., Brandner, W., Allard, F., Homeier, D., Freytag, B., Bailer-Jones, C. A. L., Greiner, J., Henning, T., & Goldman, B. 2013, *ApJ*, 778, L10
- Boffin, H. M. J., Pourbaix, D., Mužić, K., Ivanov, V. D., Kurtev, R., Beletsky, Y., Mehner, A., Berger, J. P., Girard, J. H., & Mawet, D. 2014, *A&A*, 561, L4
- Buenzli, E., Marley, M. S., Apai, D., & Lupu, R. E. 2014, *Mem. Soc. Astron. Italiana*, 85, 690
- Buenzli, E., Marley, M. S., Apai, D., Saumon, D., Biller, B. A., Crossfield, I. J. M., & Radigan, J. 2015a, *ApJ*, 812, 163
- Buenzli, E., Saumon, D., Marley, M. S., Apai, D., Radigan, J., Bedin, L. R., Reid, I. N., & Morley, C. V. 2015b, *ApJ*, 798, 127
- Burgasser, A. J., Gillon, M., Faherty, J. K., Radigan, J., Triaud, A. H. M. J., Plavchan, P., Street, R., Jehin, E., Delrez, L., & Opitom, C. 2014, *ApJ*, 785, 48
- Burgasser, A. J., Sheppard, S. S., & Luhman, K. L. 2013, *ApJ*, 772, 129
- Burrows, A., Heng, K., & Nampaisarn, T. 2011, *ApJ*, 736, 47
- Colón, K. D., Ford, E. B., Redfield, S., Fortney, J. J., Shabram, M., Deeg, H. J., & Mahadevan, S. 2012, *MNRAS*, 419, 2233
- Crossfield, I. J. M., Biller, B., Schlieder, J. E., Deacon, N. R., Bonnefoy, M., Homeier, D., Allard, F., Buenzli, E., Henning, T., Brandner, W., Goldman, B., & Kopytova, T. 2014, *Nature*, 505, 654
- Faherty, J. K., Beletsky, Y., Burgasser, A. J., Tinney, C., Osip, D. J., Filippazzo, J. C., & Simcoe, R. A. 2014, *ApJ*, 790, 90
- Gelman, A. & Rubin, D. B. 1992, *Stat. Sci.*, 7, 457
- Gillon, M., Triaud, A. H. M. J., Jehin, E., Delrez, L., Opitom, C., Magain, P., Lendl, M., & Queloz, D. 2013, *A&A*, 555, L5
- Karalidi, T., Apai, D., Schneider, G., Hanson, J. R., & Pasachoff, J. M. 2015, *ApJ*, 814, 65
- Kniazev, A. Y., Vaisanen, P., Mužić, K., Mehner, A., Boffin, H. M. J., Kurtev, R., Melo, C., Ivanov, V. D., Girard, J., Mawet, D., Schmidtbreick, L., Huelamo, N., Borissova, J., Minniti, D., Ishibashi, K., Potter, S. B., Beletsky, Y., Buckley, D. A. H., Crawford, S., Gulbis, A. A. S., Kotze, P., Miszalski, B., Pickering, T. E., Romero Colmenero, E., & Williams, T. B. 2013, *ApJ*, 770, 124
- Lorenz, R. D. 1998, *Planet. Space Sci.*, 47, 67
- Louden, T. & Wheatley, P. J. 2015, *ArXiv e-prints*
- Luhman, K. L. 2013, *ApJ*, 767, L1
- Mancini, L., Giacobbe, P., Littlefair, S. P., Southworth, J., Bozza, V., Damasso, M., Dominik, M., Hundertmark, M., Jørgensen, U. G., Juncher, D., Popovas, A., Rabus, M., Rahvar, S., Schmidt, R. W., Skottfelt, J., Snodgrass, C., Sozzetti, A., Alsubai, K., Bramich, D. M., Calchi Novati, S., Ciceri, S., D'Ago, G., Figueroa Jaimes, R., Galianni, P., Gu, S.-H., Harpsøe, K., Haugbølle, T., Henning, T., Hinse, T. C., Kains, N., Korhonen, H., Scarpetta, G., Starkey, D., Surdej, J., Wang, X.-B., & Wertz, O. 2015, *A&A*, 584, A104
- Metchev, S. A., Heinze, A., Apai, D., Flateau, D., Radigan, J., Burgasser, A., Marley, M. S., Artigau, É., Plavchan, P., & Goldman, B. 2015, *ApJ*, 799, 154
- Radigan, J. 2014, *ArXiv e-prints*
- Radigan, J., Lafrenière, D., Jayawardhana, R., & Artigau, E. 2014, *ArXiv e-prints*
- Sahlmann, J. & Lazorenko, P. F. 2015, *MNRAS*, 453, L103
- Saumon, D., & Marley, M. S. 2008, *ApJ*, 689, 1327
- Schwarz, G. 1978, *Annals of Statistics*, 6, 461
- Showman, A. P. & Dowling, T. E. 2000, *Science*, 289, 1737
- Showman, A. P. & Ingersoll, A. P. 1998, *Icarus*, 132, 205
- Simon, A. A., Rowe, J. F., Gaulme, P., Hammel, H. B., Casewell, S. L., Fortney, J. J., Gizis, J. E., Lissauer, J. J., Morales-Juberias, R., Orton, G. S., Wong, M. H., & Marley, M. S. 2015, *ArXiv e-prints*
- Snellen, I. A. G., de Kok, R. J., de Mooij, E. J. W., & Albrecht, S. 2010, *Nature*, 465, 1049
- Unruh, Y. C. & Collier Cameron, A. 1995, *MNRAS*, 273, 1
- Vogt, S. S., Penrod, G. D., & Hatzes, A. P. 1987, *ApJ*, 321, 496